Marine Geology 371 (2016) 120–129

Contents lists available at ScienceDirect

Marine Geology

journal homepage: www.elsevier.com/locate/margo

Submarine landslides on the Great Barrier Reef shelf edge and upper slope: A mechanism for generating tsunamis on the north-east Australian coast?

Jody M. Webster [a,*], Nicholas P.J. George [b], Robin J. Beaman [c], Jon Hill [d], Ángel Puga-Bernabéu [a,e], Gustavo Hinestrosa [a], Elizabeth A. Abbey [a], James J. Daniell [b]

[a] Geocoastal Group, School of Geosciences, The University of Sydney, NSW 2006, Australia
[b] College of Science, Technology and Engineering, James Cook University, Townsville, QLD 4811, Australia
[c] College of Science, Technology and Engineering, James Cook University, PO Box 6811, Cairns, QLD 4870, Australia
[d] Environment Department, University of York, York YO10 5DD, UK
[e] Departamento de Estratigrafía y Paleontología, Universidad de Granada, 18002 Granada, Spain

ARTICLE INFO

Article history:
Received 19 August 2015
Received in revised form 3 November 2015
Accepted 21 November 2015
Available online 23 November 2015

Keywords:
Great Barrier Reef
Continental shelf
Submarine landslides
Tsunami
Numerical model
Sea-level change

ABSTRACT

Shallow (<200 m) submarine landslides influence margin evolution and can produce devastating tsunamis, yet little is known about these processes on mixed siliciclastic–carbonate margins. We have discovered seven landslides along the shelf edge and upper slope of the central Great Barrier Reef (GBR), Australia. The largest shelf edge landslide is investigated in detail and represents a collapse of a 7 km long section of the shelf edge at 90 m water depth with coarse debris deposited up to 5.5 km away on the upper slope down to 250 m. The precise timing and triggering mechanisms are uncertain but available chronologic and seismic stratigraphic evidence suggests that this event occurred during the last deglacial sea-level rise between 20 and 14 ka. Regional bathymetric data confirms that these shelf edge and upper slope slides are restricted to the central GBR between latitude 18° and 19°S, suggesting a spatial relationship between the extensive Burdekin paleo-fluvial/delta system and shallow landslide activity. This study highlights an important local mechanism for the generation of tsunamis on this margin type, and numerical simulations under present conditions confirm that a 2 to 3 m tsunami wave could be produced locally. However, we consider that the risk of such slides, and their resulting tsunamis, to the modern coastline is negligible due to their relatively small size and the capacity of the GBR to dissipate the wave energy.

1. Introduction

Submarine landslides have the potential to shape margin structure and morphology and produce devastating tsunamis (e.g. Owen et al., 2007; Talling et al., 2014). Slides occurring in shallow water can be dangerous given their normally closer proximity to the coast and a shorter distance available for radial damping of the resulting tsunami wave (Harbitz et al., 2006; Masson et al., 2006). However, most of the studied shallow water slides come from siliciclastic-dominated margins (e.g. Palos Verdes and Goleta slides; Bohannon and Gardner, 2004; Fisher et al., 2005), isolated, pure carbonate platforms (e.g. Great Bahama Bank, Nicaraguan Rise; Hine et al., 1992; Jo et al., 2015), oceanic islands (e.g. Hawaiian, Lesser Antilles Islands; Lipman et al., 1988; Trofimovs et al., 2010) or glaciated margins (e.g. North Atlantic; Haflidason et al., 2004; Twichell et al., 2009) and they are either associated with active canyon, tectonic or volcanic processes. In contrast, little is known about shelf and upper slope failures (<200 m) on mixed siliciclastic–carbonate passive margins, despite the prevalence of these margins in the geologic record (Mount, 1984) and proximity to many modern, populated coastlines (e.g. Brazil, Australia).

The northeast Australian margin represents the largest, extant mixed siliciclastic–carbonate margin and possible tsunami deposits have been described at several localities (Bryant and Nott, 2001; Nott, 1997). Large tsunami waves up to 11 m are hypothesized to have entered the Great Barrier Reef (GBR) through deep channels and impacted the coast. However, this interpretation remains controversial for several reasons. First, it is difficult to reconcile such large tsunami waves when most of the known Australian tsunamis are thought to have an earthquake-induced origin very far from the Australian coast, generated at or near major subduction zones in the Pacific (Dominey-Howes, 2007). Second, it is poorly understood whether the presence of the GBR attenuates (Baba et al., 2008; Xing et al., 2014) or amplifies (Nott, 1997) the resulting tsunami waves. Submarine landslides along continental or oceanic margins can occur much closer to the coast, and

* Corresponding author at: Geocoastal Research Group, School of Geosciences, The University of Sydney, NSW 2006, Australia.
E-mail address: jody.webster@sydney.edu.au (J.M. Webster).

http://dx.doi.org/10.1016/j.margeo.2015.11.008
0025-3227/

despite their lower energy release compared with subduction-related earthquakes, can cause significant local to regional destruction (e.g. Storegga tsunami, Sissano, Papua New Guinea tsunamis; Bondevik et al., 2005; Bondevik et al., 1997; Tappin et al., 2001). However, until recently we have lacked the required high-resolution bathymetric data coverage to accurately identify the submarine landslides along the margin of the GBR and to evaluate their tsunamigenic potential.

Recent geomorphic investigations have identified several large (up to 20 km long) submarine landslide headscarps (Beaman and Webster, 2008; Puga-Bernabéu et al., 2011, 2013b; Webster et al., 2012) and potential slope failures along the GBR margin (Puga-Bernabéu et al., 2013a). However, these slides are mostly limited to the middle and lower slope and/or so far lack the published geomorphic constraints (i.e. slide scarp, basal surface and deposits, slide volume, run-out etc.) needed for robust assessment of their timing and tsunamigenic potential. In the last decade, following the extensive acquisition of high-resolution multibeam data, our understanding of the geomorphology of the northeast Australian shelf edge, particularly the drowned reefs, has greatly improved (Abbey et al., 2011; Hinestrosa et al., 2014). Our analysis of the most comprehensive bathymetric dataset assembled to date from the GBR margin has revealed seven shallow landslides (i.e. with headscarps at depths shallower than 200 m) along the shelf edge and upper slope of the central GBR. The largest failure of the shelf edge lies adjacent to Viper Reef, referred to hereafter as the Viper Slide (Fig 1). Here we focus on the surface and subsurface geomorphology of the Viper Slide and discuss the likely timing, pre-conditioning factors and triggering mechanisms. We also evaluate the tsunamigenic potential of the slide by performing numerical simulations aimed at assessing the risk that such an event poses to the present northeast Australian coastline.

2. Methods

2.1. Multibeam, seismic and dredge data

Swath bathymetry and backscatter data from the GBR shelf edge and upper slope were collected with a EM300 (30 kHz) multibeam echo sounder on the RV *Southern Surveyor* (Webster et al., 2008). To investigate the surface geomorphology of the Viper Slide (Figs. 1, 2), these data were processed in Caris HIPS/SIPS and QPS FMGeocoder Toolbox to produce 10 m bathymetry and 2 m backscatter grids, then analyzed to map and characterize the slide scar and deposit. The regional distribution of other shallow slides were assessed using the most comprehensive 100 m grid available for the GBR (Beaman, 2010), together with smaller 10 m grids (Fig. 1B) using the EM300 data. Eight high-resolution sub-bottom profiles were acquired across the Viper Slide using a TOPAS PS-18 (18 kHz) to identify the subsurface characteristics and determine the depositional timing based on regional seismic stratigraphic relationships (Figs. 2, 3). Samples were dredged from the top of the slide debris and radiocarbon dated (Abbey et al., 2013).

Combining all available multibeam, backscatter and seismic data, the post-slide bathymetry grid was subtracted from a pre-slide bathymetry grid in ArcGIS 3D Analyst to calculate: (1) the volume removed by the slide from the source areas (i.e. headscarp); and (2) the volume added by the slide in the depositional area down slope of the main scarp (after Volker, 2010) (Figs. 4, 5). The latter represents a simple

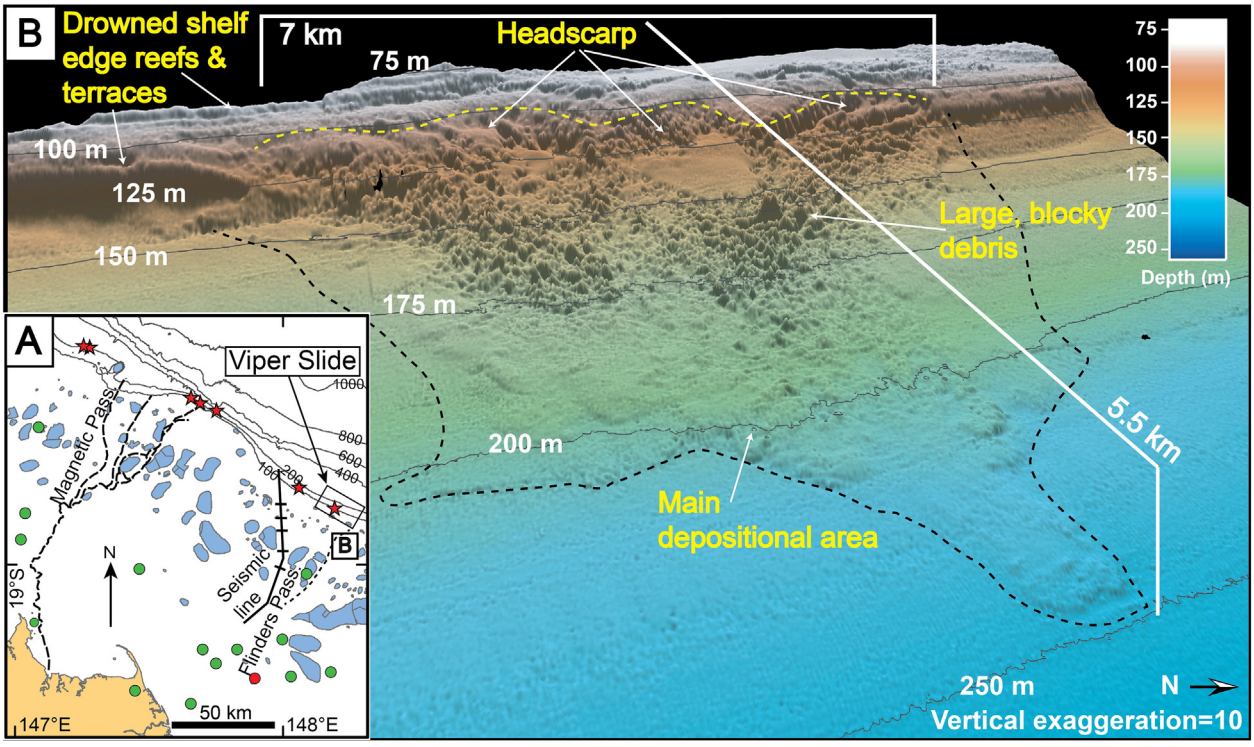

Fig. 1. (A) Map showing the distribution shelf edge and upper slope submarine landslides along the central Great Barrier Reef margin. The long black dashed lines represent the known extent of the paleo-Burdekin river system (after Fielding et al., 2003) that crosses the modern GBR shelf. The short dashed lined to the South East of Flinders Passage represents another significant paleo-channel (after Harris et al., 1990). The likely shelf expression of the corresponding lowstand paleo-Burdekin delta system is clearly marked by the slope-ward shift in the 100 and 200 m contours observed in the 100 m DEM. The red stars show the locations of shallow (<200 m) shelf edge and upper slope landslides associated with the paleo-Burdekin delta system, including the main Viper Slide study area (box inset B). Green dots represent earthquake epicenters of $1 < M_w \leq 4$ recorded in the regions since 1866–2000 (http://www.quakes.uq.edu.au), with the largest event (4.7 Mw) indicated by the red dot. Solid black line shows seismic line SS092008_019_001 on the shelf near the Viper Slide that intersects five large (up to 2 km wide) paleo-channels (black crossing lines). (B) High-resolution 3D bathymetry (10 m grid) showing the geomorphology of the Viper Slide head scarp and deposit. Multiple, arcuate indentations characterize the headscarp (yellow dashed line) and cut into the shelf edge leaving a blocky debris and wider depositional zone on the upper slope (black dashed line). Well-developed drowned shelf edge reefs (Abbey et al., 2011) are observed wrapping around the headscarp. At its widest point, the landslide scarp is about 7 km and 5.5 km long downslope to its toe. (For interpretation of the references to color in this figure legend, the reader is referred to the web version of this article.)

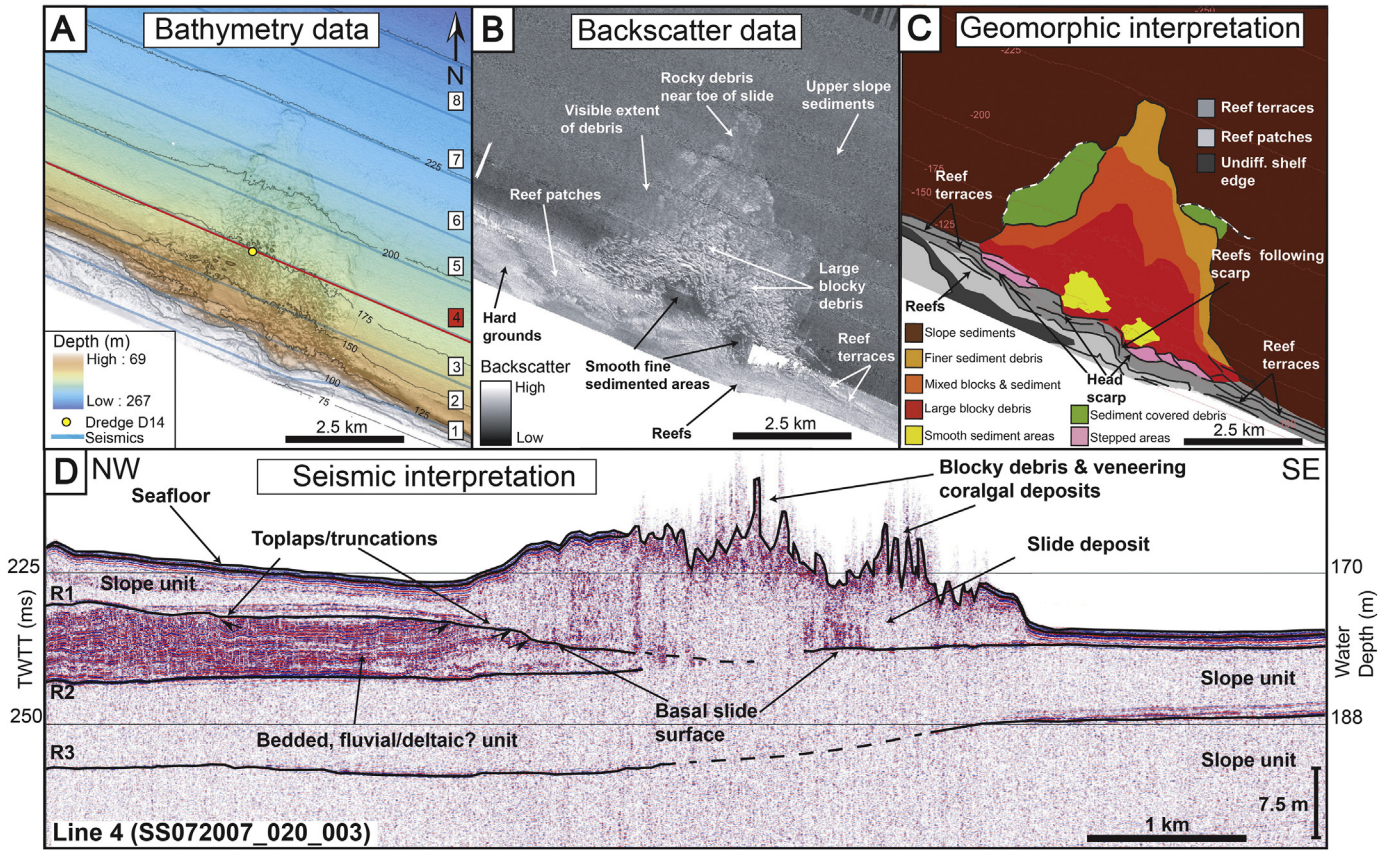

Fig. 2. (A) Landslide surface and subsurface geomorphology and interpretation. (A) Map showing the hillshaded landslide bathymetry gridded at 10 m. The locations of the nine crossing sub-bottom profiles are represented by the blue lines (see Fig. 3 for all uninterpreted and interpreted profiles). The red line depicts the key interpreted seismic section (Line 4) through the Viper Slide deposit in inset D. The yellow dot is the location of the deep-water, fossil coralline algae (Abbey et al., 2013) dredged from the top of the blocky debris zone. (B) Map showing the interpreted backscatter image gridded at 2 m of the shelf edge and landslide. (C) Geomorphic interpretation based on all the available bathymetry, backscatter and sub-bottom data. (D) Interpreted sub-bottom profile (Line 4) across the Viper Slide deposit. The maximum thickness of the deposit (~0.25 ms TWTT) is 21 to 31 m, assuming an average velocity of 1700 to 2500 m s^{-1}. The basal surface of the slide is visible within the upper slope units. Towards the northwest, this surface is clearly imaged crosscutting (i.e. toplaps/truncations) a well-bedded deposit characterized by high-amplitude, sub-parallel reflectors, and interpreted to be older fluvial/deltaic deposits associated with the paleo-Burdekin delta. The depth scale and vertical inset scale bar was estimated by assuming a p-wave velocity of 1500 m s^{-1} for sea water. (For interpretation of the references to color in this figure legend, the reader is referred to the web version of this article.)

reconstruction that projects a flat plane, relative to the adjacent undisturbed sea floor, underneath the slide deposit to form its base. This approach is justified by the uniform and continuous nature of the shelf edge terraces and upper slope on either side of the disturbed area defining the slide area. For our tsunami simulations we use a slide volume estimated from the source region (i.e. headscarp) but we also tested larger volumes to assess the sensitivity of the model.

2.2. Landslide and tsunami modeling

Numerical modeling of tsunamis generated from landslides has been carried out using a rigid block to simulate the slide (e.g. Harbitz, 1992; Løvholt et al., 2005). Three arcuate indentations are observed in the Viper Slide headscarp (Fig. 1) but available surface and subsurface geomorphic data point to a single failure event (Section 3.1), consistent with our approach to model the slide as a single block. Here, we used the finite element numerical model Fluidity (Piggott et al., 2008), to simulate the Viper Slide and resulting tsunami (see Table 1 for input parameters). This model has been used successfully to study ancient tsunamis in the Mediterranean (Shaw et al., 2008), the Storegga slide (Hill et al., 2014) and the 2011 Tohoku event (Oishi et al., 2013).

Fluidity solves the Navier–Stokes equation on a multiscale tetrahedral mesh using finite element methods. The top surface uses the novel implicit free surface algorithm of Funke et al. (2011) with drag boundary conditions, using a constant drag coefficient, on the sea bed and coastlines. The slide was parameterized using a smoothed exponential function with a total volume of 24,773,625 m^3 (0.025 km^3) (Section 3.1) and moved downslope a distance of 10 km with a prescribed acceleration, to a maximum speed (35 m/s), followed by a deceleration phase in a north-easterly direction (Table 1), consistent with observed field observations. The run-out length is longer than that derived from field observation to ensure a smoother initial acceleration for numerical purposes. The difference between the observed run-out and the simulated one is accounted for in the deceleration phase, which inputs no energy to the wave. This approach is very similar to that previously used by Harbitz (1992); Løvholt et al. (2005) and Hill et al. (2014). A tetrahedral mesh covering latitude 18° to 20°S, longitude 150°E and the Australian coastline to the west, and including the distribution of all known modern reefs, with scales varying between 100 m and 10 km, was used to simulate the most likely and conservative volume of material removed by the Viper Slide from the source area (see Sections 3.1, 3.2). To assess the sensitivity of the model and account for some uncertainties in our slide volume calculations we also tested larger (by a factor of two) slide volumes (Table 1). For more details on the model equations and discretizations, see Hill et al. (2014) and AMCG, Imperial College London (2014).

2.3. Slide equations of motion

The landslide is modeled as a rigid block that has a prescribed shape and moves using a prescribed velocity function. It is based on the equations described in Harbitz (1992) and Løvholt et al. (2005). The total

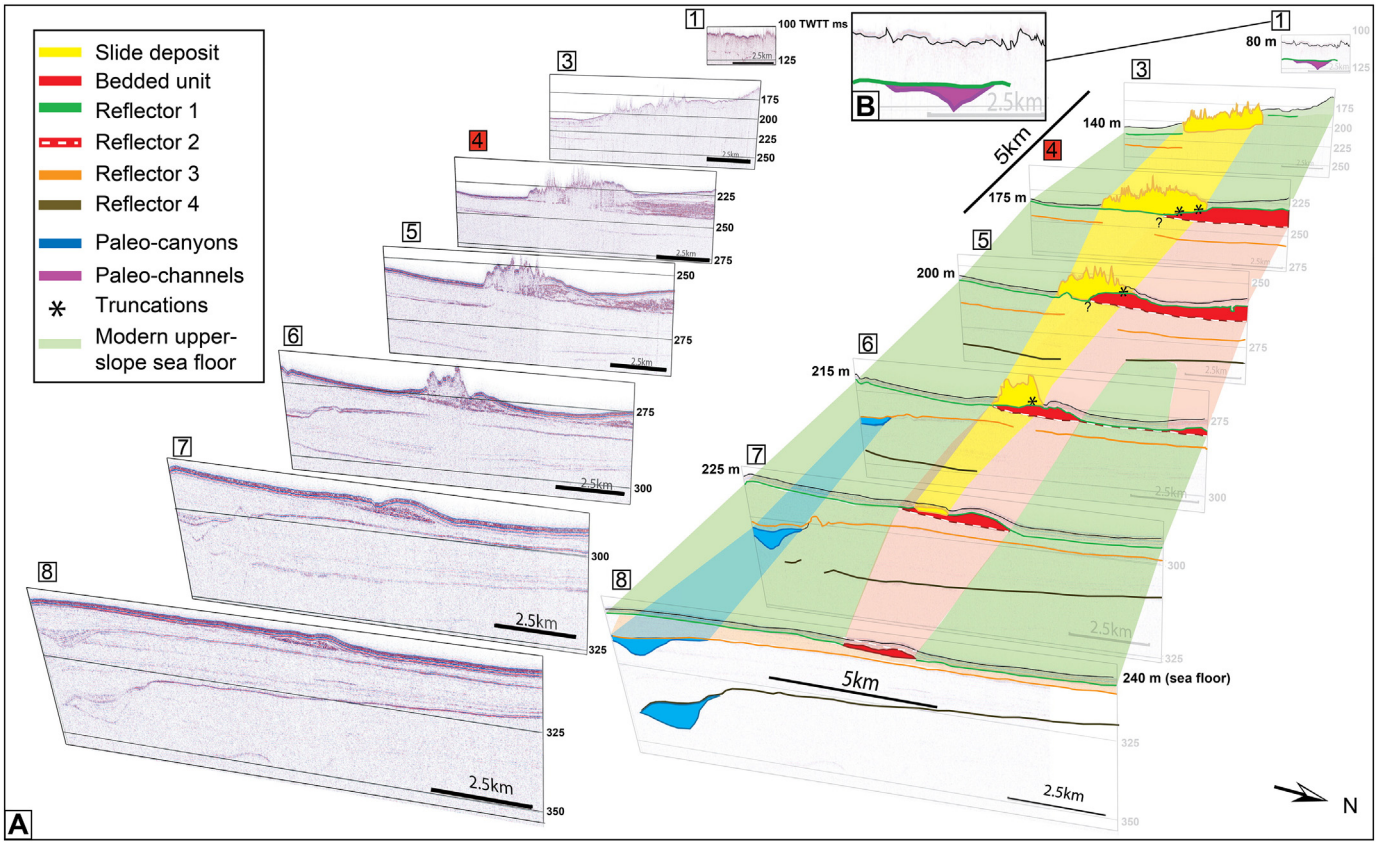

Fig. 3. (A) Uninterpreted and interpreted seismic profiles across the Viper Slide deposit on the Central GBR upper slope. The down slope distribution of the Viper Slide deposit (yellow) and key seismic reflectors are shown. The well-bedded deposits (red), characterized by high-amplitude, sub-parallel reflectors, are interpreted as fluvial/deltaic in origin and are likely associated with the paleo-Burdekin fluvial–deltaic system — the largest along the northeast Australian margin. These bedded deposits show clear evidence of erosional truncations (black stars) caused by the slide. Note the interpreted paleo-channel (pink) seen in Profile 1 (see (B) for expanded image) along the shelf edge at about 80 m depth, which may have acted as the failure surface for the slide. Successive buried paleo-canyons (blue) are also observed in Profiles 6–8 and are likely associated with the canyons heads observed distally on the upper slope in Fig. 4. The vertical scale on the profiles is in TWTT (ms) and the depth of the seafloor is also given. (For interpretation of the references to color in this figure legend, the reader is referred to the web version of this article.)

water displacement is determined by the changes in aggregated thickness as it moves with a prescribed velocity. We impose this water displacement as a normal velocity Dirichlet boundary condition on the velocity terms in the Navier–Stokes equation, $(\boldsymbol{u}\cdot\boldsymbol{n})^D$, calculated as:

$$\boldsymbol{u}\cdot\boldsymbol{n}^D = \frac{[h_s(x-x_s(t-\Delta t),y-y_s(t-\Delta t)]-[h_s(x-x_s(t),y-y_s(t)]}{\Delta t} \quad (1)$$

where Δt is the timestep of the model and $\boldsymbol{n}$ is the outward unit normal. The slide motion is described by:

$$h(x,y,t) = h_s(x-x_s(t),y-y_s(t)) \quad (2)$$

where $h(x,y,t)$ is the slide thickness in two-dimensional Cartesian space (x,y) at time t, and h_s is the water displacement (with respect to the lower boundary) of the water by the slide. The parameters x_s and y_s describe the slide motion and h_s describes the slide geometry via simple geometric relationships:

$$\left.\begin{aligned} x_s &= x_0 + s(t)\cos\phi \\ y_s &= y_0 + s(t)\sin\phi \end{aligned}\right\} 0<t<T. \quad (3)$$

Here, ϕ is the angle from the x-axis that the landslide travels in, (x_0,y_0) is the initial position of the center of the landslide headscarp. The total time of the landslide travel, T, is defined as three phases:

$$T = T_a + T_c + T_d \quad (4)$$

where T_a is the time of the acceleration phase of the slide, T_c is the time of the constant speed phase, and T_d is the time of the deceleration phase. Together with prescribed motion these govern the total run-out of the slide, R:

$$R = R_a + R_c + R_d \quad (5)$$

which is a combination of the three phases of slide movement and is governed by the travel time, defined by $T_a = \pi R_a/2U_{\max}$ (acceleration phase), $T_c = R_c/U_{\max}$ (constant speed phase) and $T_d = \pi R_d/2U_{\max}$ (deceleration phase), define the relationship between travel time, maximum speed, and run-out distance for the three phases. The term $s(t)$ in Eq. (3) governs the acceleration and deceleration phases, given a maximum slide velocity $U_{\max}$ and is defined as

Acceleration phase:

$$s(t) = R_a\left(1-\cos\left(\frac{U_{\max}}{R_a}t\right)\right), 0<t<T_a. \quad (6)$$

Constant speed phase:

$$s(t) = R_a + U_{\max}(t-T_a), T_a<t<T_a+T_c. \quad (7)$$

Deceleration phase:

$$s(t) = R_a + R_c + R_d\left(\sin\left(\frac{U_{max}}{R_d}(t-T_a-T_c)\right)\right), T_a+T_c<t<T_a+T_c+T_d. \quad (8)$$

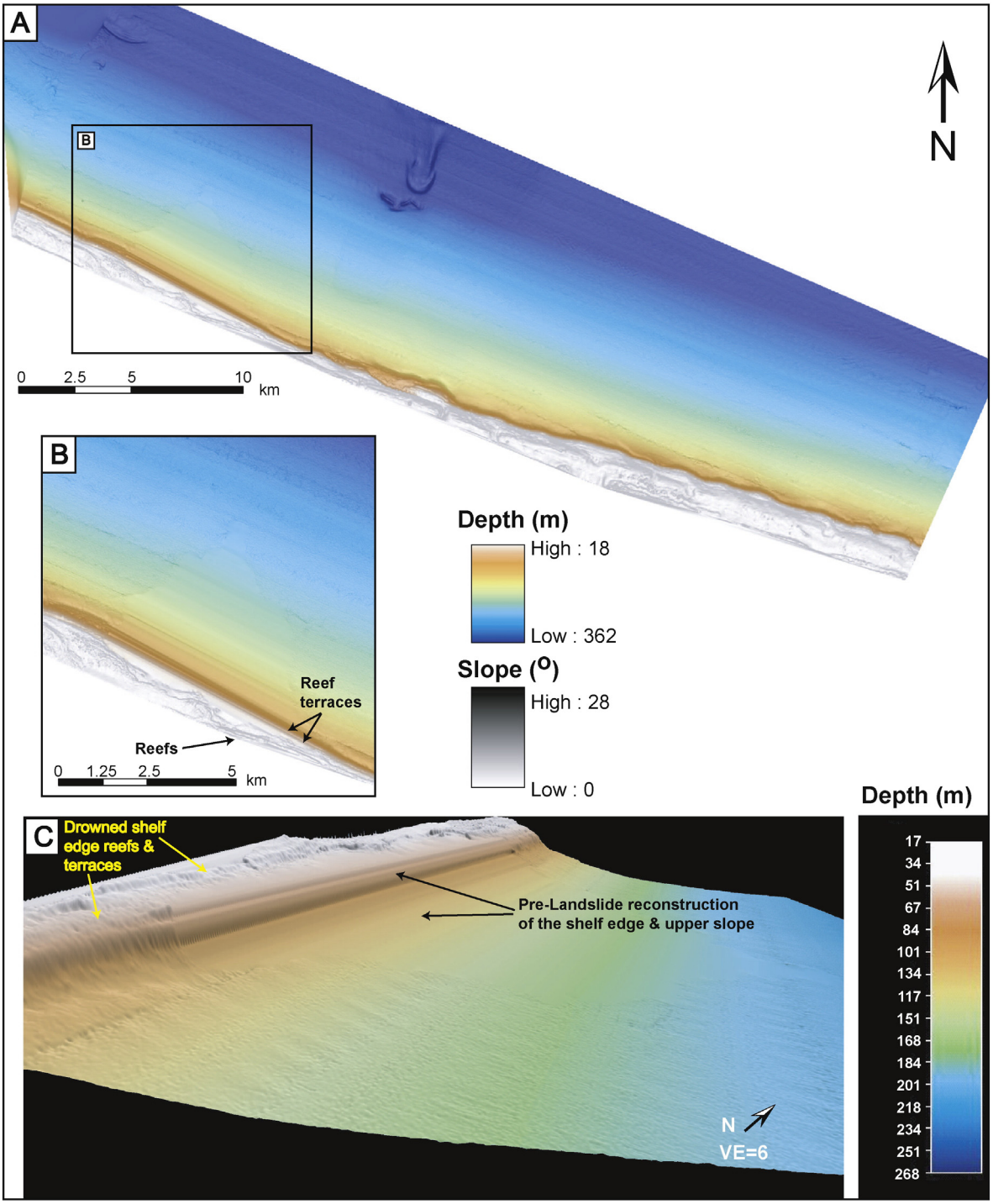

Fig. 4. Regional view showing the modeled pre-slide bathymetry. (A) The modeled surface includes the distinct terraces at −100 m and −110 m which are observed as continuous features along the shelf in this region (Abbey et al., 2011). (B) The black rectangle indicates the location of the close up of the Viper Slide site (C) The corresponding 3D view of the model. This DEM was used to calculate the landslide volume loss and gain shown in Fig. 5, as well as provide realistic inputs for the slide and tsunami numerical simulations (Table 1). VE refers to the vertical exaggeration.

The slide shape is defined as:

$$h_s = \begin{cases} h_{\max}\exp\left(-\left(2\frac{X'+S+L}{S}\right)^4-\left(2\frac{y'}{B}\right)^4\right) & \text{for} -(L+2S)<x'<-(L+S) \\ h_{\max}\exp\left(-\left(2\frac{y'}{B}\right)^4\right) & \text{for} -(L+S)\le x'<-S \\ h_{\max}\exp\left(-\left(2\frac{X'+S}{S}\right)^4-\left(2\frac{y'}{B}\right)^4\right) & \text{for} -S\le x'<0 \end{cases} \quad (9)$$

where the landslide has dimensions of maximum height, h_{max}, length, L, and width, B. To avoid sharp edges, which would cause numerical oscillations, a smoothing length, S, is used at the front and back of the slide, and the slide is smoothed along the whole width. The landslide movement is then governed by x' and y', defined by:

$$x' = (x-x_s)\cos\phi + (y-y_s)\sin\phi \quad (10)$$

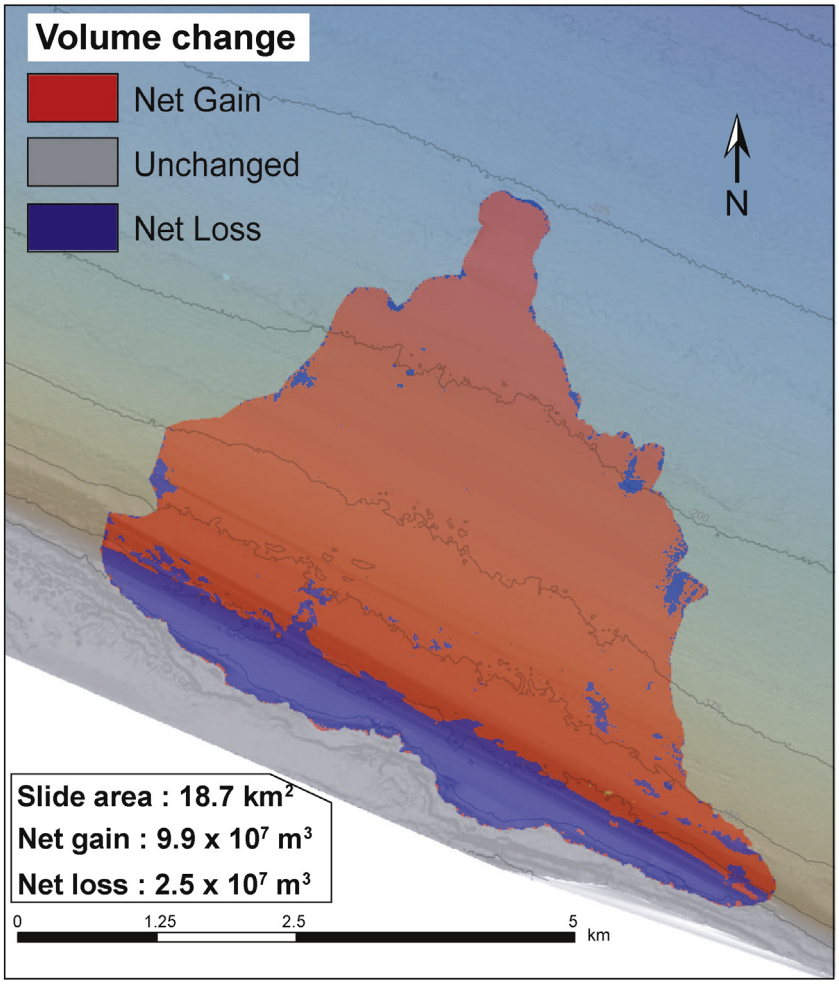

Fig. 5. Landslide volume change reconstruction. The volume of the Viper Slide was calculated by subtracting the present day bathymetry grid from a simulated prefailure bathymetric grid (Fig. 4) generated along the shelf edge and upper slope. Note the estimate of the Viper Slide area (18.7 km^2) includes both the source (blue) and depositional (red) regions. (For interpretation of the references to color in this figure legend, the reader is referred to the web version of this article.)

and

$$y' = (x - x_s)\sin\phi + (y - y_s)\cos\phi. \quad (11)$$

This gives a total volume of the slide, V:

$$V = 0.9Bh_{max}(L + 0.9S). \quad (12)$$

The parameters used in this study are given in Table 1.

Table 1
Key landslide and numerical model input parameters used for the tsunami simulations.

Parameter	Value
V — slide volume	0.025 km^3, 0.05 km^3 or 0.097 km^3
R — run out distance	10 km
L — slide length	0.025 km^3: 300 m, 0.05 km^3: 485 m, 0.097 km^3: 250 m
B — slide width	0.025 km^3: 2000 m, 0.05 km^3: 4750 m, 0.097 km^3: 4550 m
S — slide smoothing distance	0.025 km^3: 275 m, 0.05 km^3: 105 m, 0.097 km^3: 250 m
H_{max} — slide maximum height	26 or 50 m (0.025 km^3 volume only)
U_{max} — slide maximum velocity	35 m/s (25 m/s for "slow" simulation)
φ— angle of propagation from x-axis (easting)	45
Acceleration distance	5 km
Distance at maximum velocity	0 m
Deceleration distance	5 km

3. Results

3.1. Landslide geomorphology

The Viper Slide (including source and depositional regions) covers a total area of 18.7 km^2, with a maximum runout distance of 5.5 km and a mean headwall height of ~26 m from the top of the headscarp at the shelf edge (Figs. 1B, 2A–C), and forms a classic triangular shape (Masson et al., 2006). The source area is characterized by a 7 km headscarp that can be traced along the shelf edge with a sinuous shape and three well-defined arcuate indentations (Vanneste et al., 2006) at the same depth of about 90 m. The fossil reef terraces (Abbey et al., 2011; Hinestrosa et al., 2014) between 80 and 100 m continue along the unaffected shelf but are interrupted by the headscarp that locally form stepped areas with steep gradients of 7° to 10°. A sequence of shallower drowned reefs in water depth of less than 80 m wrap continuously around the headscarp (Abbey et al., 2011). Downslope, the Viper Slide deposit is characterized by blocky debris, easily distinguished from the smooth upper slope sediments (Figs. 1B, 2B, C). Bathymetry and backscatter data reveal a clear progression with increasing distance from the headscarp, from large blocky debris (up to 10,000 m^2, 17 m high) to finer debris distally, consistent with other studies (Masson et al., 2006).

Seismic profiles across the Viper Slide clearly image the headscarp, slide deposit and basal slide surface along most of its length (Figs. 2D, 3). The Viper Slide deposit is identifiable as a unit with

transparent seismic facies (Fig. 3, yellow unit) with a maximum thickness of 0.25 ms TWTT, or ~21 to 31 m assuming an average velocity of 1700 to 2500 m s^{-1} (Hinestrosa et al., 2014). This seismic facies is similar to that observed in other landslides composed of large, coherent blocks (Fanetti et al., 2008; Lastras et al., 2004). The sub-bottom profile data across the Viper Slide deposit shows the basal surface of the slide (i.e. bounding the transparent seismic facies) is visible within the upper slope unit (Figs. 2D, 3). Towards the northwest, this surface is also clearly imaged crosscutting, via toplaps and truncations, a well-bedded unit characterized by high-amplitude, sub-parallel reflectors (Fig. 3, red unit). Seismic profiles (SS092008_019_001) crossing the shelf and upper slope adjacent to Flinders and Magnetic passages (Fig. 1A) confirm the regional distribution of this unit type, and that well developed, prograding clinoforms are a key feature of this seismic unit. Taken together, this seismic unit clearly pre-dates the slide event and likely represents older fluvial/deltaic deposits associated with the paleo-Burdekin fluvial/deltaic system (Fielding et al., 2003; Harris et al., 1990; Symonds et al., 1983).

3.2. Landslide volume estimate

We estimate the volume of the Viper Slide to be 0.025 km^3, based on the total loss of material from the source area (i.e. the headscarp). This is in contrast to our estimates of the total gain of the Viper Slide deposition area of 0.099 km^3 (Fig. 5). Regardless, both of these volumes are very small when compared to giant submarine landslides, such as the Storegga slide, which involved >3000 km^3 (Haflidason et al., 2004), but similar for example to those documented by Chaytor et al. (2009) on the US continental shelf and upper slope. In the case of the Viper Slide, it is difficult to fully reconcile the difference between the estimated net loss in the source area and gain in the depositional area without additional seismic coverage and sample data. However, this may be partly explained by the erosive nature of the slide, with at least 10 m of sediments removed from beneath the basal surface of the slide in places (Figs. 2D, 3). Therefore the slide could have incorporated significant upper slope sediments within the slide depositional area. This excavation and accumulation of older upper slope sediments, combined with subsequent coralgal accretion (Abbey et al., 2013) on top of the largest slide blocks, and further upper slope sedimentation (Figs. 2B, C) after the collapse event, could explain this difference. A similar situation – albeit on a larger scale – has occurred off the Nicaraguan Rise (Hine et al., 1992), with light-dependent *Halimeda* bioherms forming significant accumulations on top of displaced blocks derived from the adjacent low-relief shallow water carbonate platform. We acknowledge the uncertainty in constraining the true effective Viper Slide volume (after Iglesias et al., 2012), and therefore use the most accurate and conservative estimate of the volume derived from the material lost directly from the headscarp (0.025 km^3) for our numerical tsunami simulations but have also tested the effect of larger slide volumes (0.05 km^3 and 0.097 km^3) and a slower moving slide (25 m/s) (Table 1).

3.3. Tsunami modeling

To investigate the impact of the Viper Slide occurring at different times and paleo-sea-level conditions, we modeled three different paleo-sea-level scenarios: 0 m (highstand), −50 m (deglacial/stadial/interstadial) and −70 m (deglacial/stadial/interstadial) (Fig. 6 and Supplementary Videos 1–4). The paleo-sea-level scenarios (−50 to −70 m) encompass most of the time that the shelf edge was submerged during the Late Pleistocene (Abbey et al., 2011). Shelf edge collapse during paleo-sea-levels lower than this (i.e. LGM when the shelf was exposed; Lambeck et al., 2014) was not considered in this simulation but we concede that this is possible, albeit unlikely given the available data (Sections 3.1, 4.1). Previous investigations of partially subaerial landslides on the flanks of fjords (Vardy et al., 2012) and volcanoes (Lipman et al., 1988) tend to produce very large tsunamis and local run-ups. However, in the case of the Viper Slide the H/L ratio (maximum headscarp height versus toe length) is consistent with other submarine landslides (Locat and Lee, 2002), and the fact that most of subaerial rock avalanches and rock slides have pancake to fan shapes (Strom, 2006), all point towards a fully marine slide.

3.3.1. 0 m sea-level scenario (highstand)

This scenario simulates the impact of the Viper Slide if it occurred during the Last Interglacial (~125 ka), or significantly, if a similar sized slide were to occur on the shelf edge today. The results show that maximum wave heights occur in the immediate vicinity of the slide and in the slide direction as expected, with some propagation along the reef front (Fig. 6A, B) to the south-east. Maximum heights are around 2 m immediately following slide initiation and rapidly decrease away from the slide region. The landward propagating wave is immediately damped by the network of shallow reefs on the shelf such that the maximum wave height reaching the present coast is only around 10 to 15 cm. Assumptions have been made on the acceleration and run-out of the slide, but sensitivity tests (see Table 1) varying the unknown parameters (not shown) give the same general conclusion. An increase in slide volume by a factor of two results in a slightly larger wave at the coastline, but still only 15 to 20 cm in height. The shallow water of the numerous reef tops dissipates energy from a wave generated in the immediate vicinity of the seaward reefs by a submarine slide of this type and scale. Only a much larger slide and/or the complete absence of the blocking effect of the GBR would generate significant wave heights at the coastline.

3.3.2. −50 m sea-level scenario (deglacial/stadial/interstadial)

The effect of the slide event occurring when sea-level was −50 m is modeled in Fig. 6C, D. In this scenario increased wave heights are observed on the small coral islands immediately landwards of the slide. These wave heights are up to 2 m on some reef islands and averaging 0.5 m for around 50 km to the north-east and south-west of the slide location.

3.3.3. −70 m sea-level scenario (deglacial/stadial/interstadial)

A further 20 m sea-level drop to −70 m moves the paleo-coast to the immediate vicinity of the slide (Fig. 6E, F). As a result, wave heights peak at up to 3 m immediately behind the slide. Additionally, wave heights remain consistently above 1 m to the south-west of the slide for 100 km along the coast. Smaller wave heights, sub-meter in scale, occur to the north-east of the slide, due to the presence of a lagoon and consequently a wider expanse of shallow water in this region.

4. Discussion

4.1. Landslide timing, pre-conditioning factors and triggering mechanisms

Based on four lines of evidence, we constrain the timing of the Viper Slide failure to between about 14 ka and 20 ka or the Last Glacial Maximum (LGM). First, a minimum age is provided by ^{14}C-AMS data (14.01 ± 0.4 ka, n = 2; Abbey et al., 2013) from fossil, deep-water (>60 m paleo-water depth) coralline algae crusts dredged in situ from the top (166 ± 7 m) of the blocky debris field (Fig. 2A). Taking into account relative sea-level (Lambeck et al., 2014) at the time, this suggests that the Viper Slide must have occurred prior to 14 ka given the paleo-water depth/age relationships (i.e. the life habitat of the dated algae is too deep), and considering that no other mass movement has occurred in the area since. Second, the spatial distribution of shelf edge reef terraces at depths between 90 to 110 m have been interrupted or broken by the headscarp, while in depths <80 m the drowned reefs wrap around scarp (Figs. 1, 2). The shelf edge reef structures have not been cored in this area so their age is unknown. However, well-dated drill transects through the same features off Cairns and Mackay recovered during IODP Expedition 325 support this timing, i.e. that the shallower,

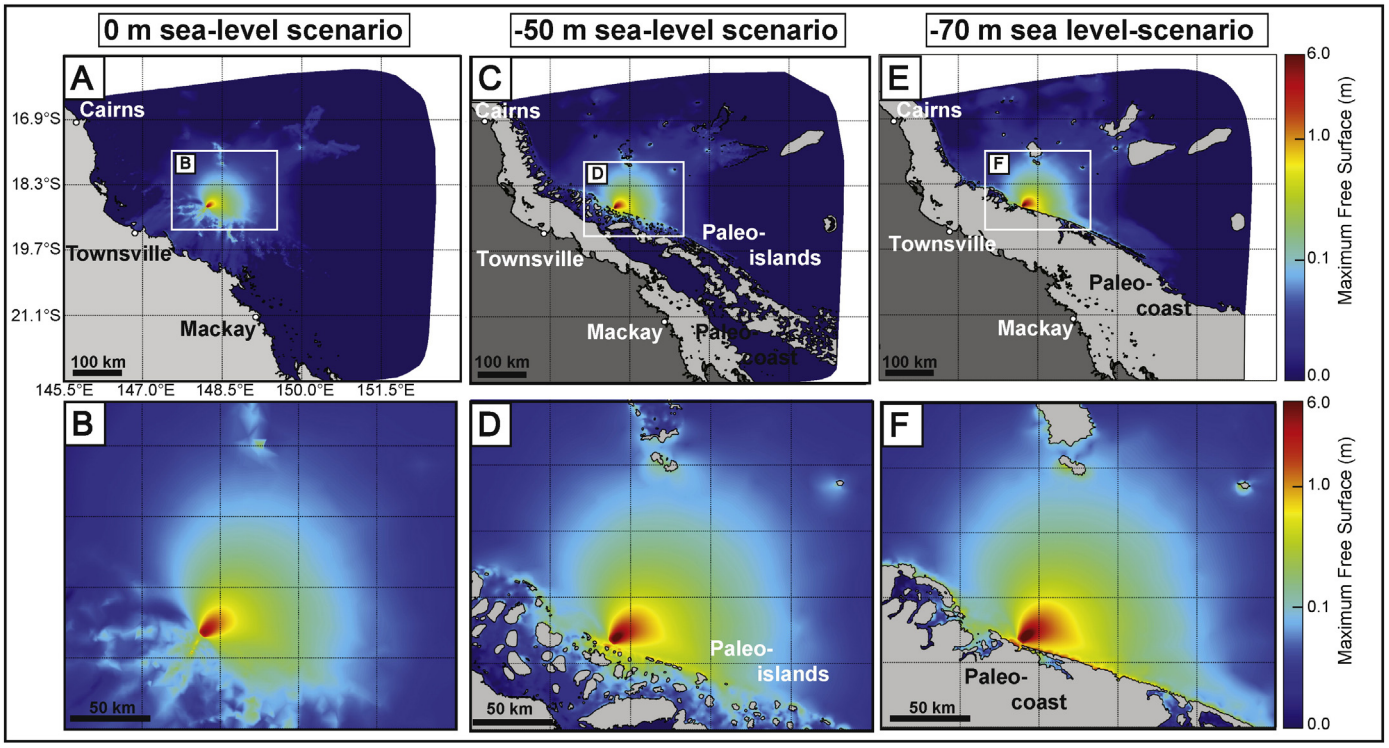

Fig. 6. Landslide and tsunami simulations of the Viper Slide. The colors represent the maximum sea surface height (or tsunami wave height) attained by the model as it radiates out from the site of the landslide. The light gray shows the estimated land surface or coast at the time of the slide, while the dark gray shows the present day coastline. (A) Numerical simulation of the Viper Slide occurring at 0 m representing collapse if it occurred at the present day, or another high sea-level period such as the Last Interglacial. (B) Close up showing backward propagating wave being damped by the network of shallow reefs on the shelf allowing only 10 to 15 cm wave to strike the coast. (C) Numerical simulation of the Viper Slide occurring at −50 m representing collapse at lower sea-levels (e.g. deglacials, interstadials/stadials). (D) Close up showing the wave heights at up to 3 m striking the much closer paleo-coast. (E) Numerical simulation of the Viper Slide occurring at −70 m representing collapse at lower sea-levels (e.g. deglacials, interstadials/stadials). (F) Close up showing the wave heights at up to 3 m striking the much closer paleo-coast. See Supplementary Videos 1–4 showing animations of these scenarios and including a test with a larger slide volume (ie. 0.097 km^3). (For interpretation of the references to color in this figure legend, the reader is referred to the web version of this article.)

post-slide reefs have grown since ~14 ka (Felis et al., 2014; Hinestrosa et al., 2014). Third, the slide clearly postdates the fluvial/deltaic deposits preserved on the upper slope (Fig. 2D) that have been interpreted regionally (Harris et al., 1990; Symonds et al., 1983) as forming during lower sea-levels (~120 m) associated with the LGM. And fourth, the morphology of the slide (i.e. shape, height and length) (Locat and Lee, 2002; Strom, 2006), while not conclusive by itself, it is consistent with failure under submarine conditions and not during periods when the shelf edge was fully exposed, such as the LGM. Taken together, these data indicate the Viper Slide may have occurred between 14 to 20 ka, perhaps following the rapid sea-level rise during meltwater pulse 1A (~14.7 ka) (Deschamps et al., 2012) but we acknowledge the assumptions implicit in this timing estimate.

Understanding submarine landslide pre-conditioning factors and triggering mechanisms is unquestionably challenging (Canals et al., 2004; Owen et al., 2007; Talling et al., 2014). In the case of the Viper Slide and the other shallow slides, several clues can be derived from their distribution along the margin, their regional depositional context and our best estimate of the slide timing. Including the Viper Slide, we have mapped seven shallow slides in the central GBR between latitude 18° to 19°S (Fig. 1B), and the available regional, high-resolution bathymetry evidence (Abbey et al., 2011; Beaman, 2010; Hinestrosa et al., 2014; Puga-Bernabéu et al., 2013a; Puga-Bernabéu et al., 2013b) suggests they are not found elsewhere on the shelf and upper slope of the GBR. This indicates a spatial link between shallow landslide activity and the paleo-Burdekin fluvial/deltaic system — the largest along the northeast Australian margin (Fielding et al., 2003). In addition to the fluvial–deltaic deposits directly beneath the Viper Slide, we imaged a paleo-channel below the sea bed on the shelf edge at 80 m (Profile 1) just landward of the main head scarp (Fig. 3). The combination of overpressure caused by rapid sedimentation and presence of weak layers (i.e. muds) acting as failure surfaces could be important preconditioning factors for the Viper Slide inception, a scenario commonly seen in siliciclastic-dominated, shelf edge fluvial–deltaic systems (Bohannon and Gardner, 2004; Fisher et al., 2005; Hampton et al., 1996).

Many submarine landslides are thought to be triggered by large earthquakes. However, based on a review of all recorded earthquakes in the region (Fig. 1A), an earthquake trigger alone, under static conditions, is difficult to reconcile as the largest event is <5 Mw. This is consistent with the modeling work by Puga-Bernabéu et al. (2013a) off Cairns, suggesting that an earthquake of >6 Mw would be required before the upper slope, albeit deeper at 400 m, would potentially fail. Additional or compounding factors are therefore required to explain the triggering mechanism of the Viper Slide. Given our estimates of the timing of the slide (14 to 20 ka), it is tantalizing to suggest that abrupt sea-level rise (~12 to 22 m) during meltwater pulse 1A (~14.7 ka) could be a contributing factor. Numerous studies have argued that there is a causal relationship between the increased frequency of landslides and this period of rapid sea-level rise, through a variety of associated forcing mechanisms (e.g. increased sedimentation, increase pore pressure, gas hydrate dissociation, increased seismicity; Brothers et al., 2013; Owen et al., 2007). However, a recent review by Urlaub et al. (2013) concluded that the link between rapid sea-level rise and submarine landslides is still unclear, and therefore our numerical simulations of the Viper Slide and resulting tsunami were carried out at different sea-levels (0 m, −50 m and −70 m).

4.2. Implications for tsunami generation and coastal impact

Our numerical simulations confirm that these shallow submarine landslides represent an important new local mechanism for the

generation of tsunami waves (up to 6 m) on this margin type (Fig. 6). However, while simulations under present or highstand conditions (~0 m sea-level) show that a 2 to 3 m wave is produced locally at the site of the slide, the model predicts only decimeter-height waves at the adjacent coastline. In contrast, the −70 m simulation shows large, meter-scale waves impacting the then proximal paleo-coast directly. Similarly in the −50 m simulation, waves of 2 to 3 m reach a number of small emergent islands and indented bays close to the slide, however, like the 0 m sea-level modeling scenario, the paleo-coast itself experiences only decimeter-scale waves.

Previous work considered the impact of tsunamis on the GBR coastline in an attempt to reconcile the presence of large boulders (Nott, 1997) and other sedimentary deposits (Bryant and Nott, 2001). While it is often difficult to categorically rule out cyclones or storms as the primary cause (Kortekaas and Dawson, 2007), these previous studies speculated that submarine slides might be a source of tsunamis on this coast. However, at the time no evidence of suitable local mass wasting deposits had been found (Bryant and Nott, 2001). Our findings suggest that these types of shallow, and comparatively small slides, are not the origin of the interpreted tsunami deposits observed on the GBR coast. However, more data are needed to assess the tsunamigenic potential of the deeper and much larger submarine landslides (Beaman and Webster, 2008; Puga-Bernabéu et al., 2013a) along the GBR margin and whether they are responsible for these deposits.

Furthermore, while not always the case at other reef-dominated margins (Chatenoux and Peduzzi, 2007), it appears that the dense matrix of coral reefs in the GBR might play a role in protecting the coastline from large tsunamis under present sea-level conditions (Baba et al., 2008; Kunkel et al., 2006; Xing et al., 2014). Our simulations show that the Viper Slide could have generated a wave of 2 to 3 m locally, but little of that energy arrived at the coastline, primarily due to its dissipation across the shelf and reef matrix. This implies that the state of the coral reef plays an important part in assessing tsunami risk, not only in terms of slide generation but also coastal protection.

Our investigation confirms that the future tsunamigenic risk to the northeast Australian coastline and built infrastructure posed by these types of small, relatively shallow slides is negligible. Intriguingly, the numerical tsunami modeling at lower sea-level positions (−50 m and −70 m) provides a tantalizing glimpse into what indigenous people living on the shelf at the time, on what was then a coastal plain, might have faced (i.e. sudden devastating meter-scale tsunamis at the shoreline). Aboriginal mythology is rich in dream-time stories of rapid and catastrophic floods (Nunn, 2014), that until now, have been ascribed primarily to the deglacial sea-level rise.

5. Conclusions

Shallow submarine landslides (<200 m) are restricted to the central GBR margin between latitude 18° to 19°S, suggesting a relationship between the location of the paleo-Burdekin fluvial/deltaic system and shallow landslide activity. We investigated the largest shelf edge landslide (18 km^2, 0.025 km^3) and concluded this event occurred during the last deglacial (14 to 20 ka). Preconditioned in some way by their proximity to a large paleo-fluvial/deltaic system, these shallow slides represent an important local mechanism for the generation of tsunamis on this mixed siliciclastic–carbonate margin type. Numerical simulations confirm a 2 to 3 m wave is produced locally but the risk to the modern coastline is negligible due to the apparent capacity of the GBR to dissipate the wave energy. Future work must now focus on systematically understanding the preconditioning factors, triggering mechanisms and the tsunamigenic potential of the deeper and larger submarine landslides along the northeastern Australian margin, while better quantifying what role the reefs of the GBR play in attenuating tsunamis.

Supplementary data to this article can be found online at http://dx.doi.org/10.1016/j.margeo.2015.11.008.

Acknowledgments

We thank the Australia's Marine National Facility (SS07/2007), the Australian Research Council (DP1094001), and NERC (NE/K000047/1). We are indebted to Peter Davies for his contributions during the cruise and advice on the analysis of the seismic data. We also thank Galderic Lastras, Albert C. Hine, and an anonymous reviewer for their constructive reviews of earlier versions of the manuscript.

References

Abbey, E., Webster, J.M., Beaman, R.J., 2011. Geomorphology of submerged reefs on the shelf edge of the Great Barrier Reef: the influence of oscillating Pleistocene sea-levels. Mar. Geol. 288 (1-4), 61–78.
Abbey, E., Webster, J.M., Braga, J.C., Jacobsen, G.E., Thorogood, G., Thomas, A.L., Camoin, G., Reimer, P.J., Potts, D.C., 2013. Deglacial mesophotic reef demise on the Great Barrier Reef. Palaeogeogr. Palaeoclimatol. Palaeoecol. 392, 473–494.
AMCG, 2014. Fluidity manual v4.1.11: Imperial College London. http://dx.doi.org/10.6084/m9.figshare.995912.
Baba, T., Mleczko, R., Burbidge, D., Cummins, P.R., Thio, H.K., 2008. The effect of the Great Barrier Reef on the propagation of the 2007 Solomon Islands tsunami recorded in Northeastern Australia. Pure Appl. Geophys. 165 (11-12), 2003–2018.
Beaman, R.J., 2010. 3DGBR: A High-resolution Depth Model for the Great Barrier Reef and Coral Sea.
Beaman, R.J., Webster, J.M., 2008. Gloria Knolls: a new coldwater coral habitat on the Great Barrier Reef margin, Australia. In: Tracey, H.N.a.D. (Ed.), 4th International Symposium on Deep-sea Corals. National Institute of Water and Atmospheric Research, Wellington, New Zealand.
Bohannon, R.G., Gardner, J.V., 2004. Submarine landslides of San Pedro Escarpment, southwest of Long Beach, California. Mar. Geol. 203 (3-4), 261–268.
Bondevik, S., Løvholt, F., Harbitz, C., Mangerud, J., Dawson, A., Inge Svendsen, J., 2005. The Storegga Slide tsunami—comparing field observations with numerical simulations. Mar. Pet. Geol. 22 (1–2), 195–208.
Bondevik, S., Svendsen, J.I., Mangerud, J.A.N., 1997. Tsunami sedimentary facies deposited by the Storegga tsunami in shallow marine basins and coastal lakes, western Norway. Sedimentology 44 (6), 1115–1131.
Brothers, D.S., Luttrell, K.M., Chaytor, J.D., 2013. Sea-level-induced seismicity and submarine landslide occurrence. Geology 41 (9), 979–982.
Bryant, E.A., Nott, J., 2001. Geological indicators of large tsunami in Australia. Nat. Hazards 24 (3), 231–249.
Canals, M., Lastras, G., Urgeles, R., Casamor, J.L., Mienert, J., Cattaneo, A., De Batist, M., Haflidason, H., Imbo, Y., Laberg, J.S., Locat, J., Long, D., Longva, O., Masson, D.G., Sultan, N., Trincardi, F., Bryn, P., 2004. Slope failure dynamics and impacts from seafloor and shallow sub-seafloor geophysical data: case studies from the COSTA project. Mar. Geol. 213 (1–4), 9–72.
Chatenoux, B., Peduzzi, P., 2007. Impacts from the 2004 Indian Ocean tsunami: analysing the potential protecting role of environmental features. Nat. Hazards 40 (2), 289–304.
Chaytor, J.D., ten Brink, U.S., Solow, A.R., Andrews, B.D., 2009. Size distribution of submarine landslides along the U.S. Atlantic margin. Mar. Geol. 264 (1-2), 16–27.
Deschamps, P., Durand, N., Bard, E., Hamelin, B., Camoin, G., Thomas, A.L., Henderson, G.M., Okuno, J.i., Yokoyama, Y., 2012. Ice-sheet collapse and sea-level rise at the Bølling warming 14,600 years ago. Nature 483 (7391), 559–564.
Dominey-Howes, D., 2007. Geological and historical records of tsunami in Australia. Mar. Geol. 239 (1-2), 99–123.
Fanetti, D., Anselmetti, F.S., Chapron, E., Sturm, M., Vezzoli, L., 2008. Megaturbidite deposits in the Holocene basin fill of Lake Como (Southern Alps, Italy). Palaeogeogr. Palaeoclimatol. Palaeoecol. 259 (2-3), 323–340.
Felis, T., McGregor, H.V., Linsley, B.K., Tudhope, A.W., Gagan, M.K., Suzuki, A., Inoue, M., Thomas, A.L., Esat, T.M., Thompson, W.G., Tiwari, M., Potts, D.C., Mudelsee, M., Yokoyama, Y., Webster, J.M., 2014. Intensification of the meridional temperature gradient in the Great Barrier Reef following the Last Glacial Maximum. Nat. Commun., v. 5.
Fielding, C.R., Trueman, J.D., Dickinson, G.R., Page, M., 2003. Anatomy of the buried Burdekin River channel across the Great Barrier Reef shelf: how does a major river operate on a tropical mixed siliciclastic/carbonate margin during sea level lowstand? Sediment. Geol. 157, 291–301.
Fisher, M.A., Normark, W.R., Greene, H.G., Lee, H.J., Sliter, R.W., 2005. Geology and tsunamigenic potential of submarine landslides in Santa Barbara Channel, Southern California. Mar. Geol. 224 (1-4), 1.
Funke, S.W., Pain, C.C., Kramer, S.C., Piggott, M.D., 2011. A wetting and drying algorithm with a combined pressure/free-surface formulation for non-hydrostatic models. Adv. Water Resour. 34 (11), 1483–1495.
Haflidason, H., Sejrup, H.P., Nygård, A., Mienert, J., Bryn, P., Lien, R., Forsberg, C.F., Berg, K., Masson, D., 2004. The Storegga Slide: architecture, geometry and slide development. Mar. Geol. 213 (1–4), 201–234.
Hampton, M.A., Lee, H.J., Locat, J., 1996. Submarine landslides. Rev. Geophys. 34 (1), 33–59.
Harbitz, C.B., 1992. Model simulations of tsunamis generated by the Storegga Slides. Mar. Geol. 105 (1–4), 1–21.
Harbitz, C.B., Lovholt, F., Pedersen, G., Masson, D.G., 2006. Mechanisms of tsunami generation by submarine landslides: a short review. Nor. J. Geol. 86, 255–264.
Harris, P.T., Davies, P.J., Marshall, J.F., 1990. Late Quaternary sedimentation on the Great Barrier Reef continental shelf and slope east Townsville, Australia. Mar. Geol. 94, 55–77.

Hill, J., Collins, G.S., Avdis, A., Kramer, S.C., Piggott, M.D., 2014. How does multiscale modelling and inclusion of realistic palaeobathymetry affect numerical simulation of the Storegga Slide tsunami? Ocean Model. 83 (0), 11–25.
Hine, A.C., Locker, S.D., Tedesco, L.P., Mullins, H.T., Hallock, P., Belknap, D.F., Gonzales, J.L., Neuman, A.C., Snyder, S.W., 1992. Megabreccia shedding from modern, low-relief carbonate platforms, Nicaraguan Rise. Geol. Soc. Am. Bull. 104 (8), 928–943.
Hinestrosa, G., Webster, J.M., Beaman, R.J., Anderson, L.M., 2014. Seismic stratigraphy and development of the shelf-edge reefs of the Great Barrier Reef, Australia. Mar. Geol. 353 (0), 1–20.
Iglesias, O., Lastras, G., Canals, M., Olabarrieta, M., González, M., Aniel-Quiroga, Í., Otero, L., Durán, R., Amblas, D., Casamor, J.L., Tahchi, E., Tinti, S., Mol, B.D., 2012. The BIG'95 submarine landslide-generated tsunami: a numerical simulation. J. Geol. 120 (1), 31–48.
Jo, A., Eberli, G.P., Grasmueck, M., 2015. Margin collapse and slope failure along southwestern Great Bahama Bank. Sediment. Geol. 317, 43–52.
Kortekaas, S., Dawson, A.G., 2007. Distinguishing tsunami and storm deposits: an example from Martinhal, SW Portugal. Sediment. Geol. 200 (3–4), 208–221.
Kunkel, C.M., Hallberg, R.W., Oppenheimer, M., 2006. Coral reefs reduce tsunami impact in model simulations. Geophys. Res. Lett. 33 (23).
Lambeck, K., Rouby, H., Purcell, A., Sun, Y., Sambridge, M., 2014. Sea level and global ice volumes from the Last Glacial Maximum to the Holocene. Proc. Natl. Acad. Sci. U. S. A.
Lastras, G., Canals, M., Urgeles, R., De Batist, M., Calafat, A.M., Casamor, J.L., 2004. Characterisation of the recent BIG'95 debris flow deposit on the Ebro margin, Western Mediterranean Sea, after a variety of seismic reflection data. Mar. Geol. 213 (1–4), 235–255.
Lipman, P.W., Normark, W.R., Moore, J.G., Wilson, J.B., Gutmacher, C.E., 1988. The giant submarine Alika debris slide, Mauna Loa, Hawaii. J. Geophys. Res. 93 (B5), 4279.
Locat, J., Lee, H.J., 2002. Submarine landslides: advances and challenges. Can. Geotech. J. 39 (1), 193–212.
Løvholt, F., Harbitz, C.B., Haugen, K.B., 2005. A parametric study of tsunamis generated by submarine slides in the Ormen Lange/Storegga area off western Norway. Mar. Pet. Geol. 22 (1–2), 219–231.
Masson, D.G., Harbitz, C.B., Wynn, R.B., Pedersen, G., Lovholt, F., 2006. Submarine landslides: processes, triggers and hazard prediction. Philos. Trans. A Math. Phys. Eng. Sci. 364 (1845), 2009–2039.
Mount, J.F., 1984. Mixing of siliciclastic and carbonate sediments in shallow shelf environments. Geology 12, 432–435.
Nott, J., 1997. Extremely high-energy wave deposits inside the Great Barrier Reef, Australia: determining the cause—tsunami or tropical cyclone. Mar. Geol. 141 (1–4), 193–207.
Nunn, P., 2014. Geohazards and myths: ancient memories of rapid coastal change in the Asia-Pacific region and their value to future adaptation. Geosci. Lett. 1 (3), 1–11.
Oishi, Y., Piggott, M.D., Maeda, T., Kramer, S.C., Collins, G.S., Tsushima, H., Furumura, T., 2013. Three-dimensional tsunami propagation simulations using an unstructured mesh finite element model. J. Geophys. Res. Solid Earth 118 (6), 2998–3018.
Owen, M., Day, S., Maslin, M., 2007. Late Pleistocene submarine mass movements: occurrence and causes. Quat. Sci. Rev. 26 (7-8), 958–978.
Piggott, M.D.G.G.J., Pain, C.C., Allison, P.A., Candy, A.S., Martin, B.T., Wells, M.R., 2008. A new computational framework for multi-scale ocean modelling based on adapting unstructured meshes. Int. J. Numer. Methods Fluids 56 (8), 1003–1015.
Puga-Bernabéu, Á., Webster, J.M., Beaman, R.J., 2013a. Potential collapse of the upper slope and tsunami generation on the Great Barrier Reef margin, north-eastern Australia. Nat. Hazards.
Puga-Bernabéu, Á., Webster, J.M., Beaman, R.J., Guilbaud, V., 2011. Morphology and controls on the evolution of a mixed carbonate–siliciclastic submarine canyon system, Great Barrier Reef margin, north-eastern Australia. Mar. Geol. 289 (1-4), 100–116.
Puga-Bernabéu, Á., Webster, J.M., Beaman, R.J., Guilbaud, V., 2013b. Variation in canyon morphology on the Great Barrier Reef margin, north-eastern Australia: the influence of slope and barrier reefs. Geomorphology 191 (0), 35–50.
Shaw, B., Ambraseys, N.N., England, P.C., Floyd, M.A., Gorman, G.J., Higham, T.F.G., Jackson, J.A., Nocquet, J.M., Pain, C.C., Piggott, M.D., 2008. Eastern Mediterranean tectonics and tsunami hazard inferred from the AD 365 earthquake. Nat. Geosci. 1 (4), 268–276.
Strom, A., 2006. Morphology and internal structure of rockslides and rock avalanches: grounds and constraints for their modelling. In: Evans, S.G., Scarascia Mugnozza, G., Strom, A.L., Hermanns, R.L. (Eds.), Landslides From Massive Rock Slope Failure. Springer-Verlag, Dordrecht, pp. 305–328.
Symonds, P.A., Davies, P.J., Parisi, R., 1983. Structure and stratigraphy of the central Great Barrier Reef: BMR J. Aust. Geol. Geophys. 8, 277–291.
Talling, P., Clare, M., Urlaub, M., Pope, E., Hunt, J., Watt, S., 2014. Large submarine landslides on continental slopes: geohazards, methane release, and climate change. Oceanography 27 (2), 32–45.
Tappin, D.R., Watts, P., McMurtry, G., Lafoy, Y., Matsumoto, T., 2001. The Sissano, Papua New Guinea tsunami. Mar. Geol. 175, 1–23.
Trofimovs, J., Fisher, J.K., Macdonald, H.A., Talling, P.J., Sparks, R.S.J., Hart, M.B., Smart, C.W., Boudon, G., Deplus, C., Komorowski, J.-C., Le Friant, A., Moreton, S.G., Leng, M.J., 2010. Evidence for carbonate platform failure during rapid sea-level rise; ca 14 000 year old bioclastic flow deposits in the Lesser Antilles. Sedimentology 57 (3), 735–759.
Twichell, D.C., Chaytor, J.D., ten Brink, U.S., Buczkowski, B., 2009. Morphology of late Quaternary submarine landslides along the U.S. Atlantic continental margin. Mar. Geol. 264 (1-2), 4–15.
Urlaub, M., Talling, P.J., Masson, D.G., 2013. Timing and frequency of large submarine landslides: implications for understanding triggers and future geohazard. Quat. Sci. Rev. 72, 63–82.
Vanneste, M., Mienert, J., Bunz, S., 2006. The Hinlopen Slide: a giant, submarine slope failure on the northern Svalbard margin, Arctic Ocean. Earth Planet. Sci. Lett. 245 (1-2), 373–388.
Vardy, M.E., L'Heureux, J.-S., Vanneste, O.L., Steiner, A., Forsberg, C., Haflidason, H., Brendryen, J., 2012. Multidisciplinary investigation of a shallow near-shore landslide, Finneidfjord, Norway. Near Surf. Geophys. 10 (4), 267–277.
Volker, D.J., 2010. A simple and efficient GIS tool for volume calculations of submarine landslides. Geo-Mar. Lett. 30 (5), 541–547.
Webster, J.M., Beaman, R.J., Bridge, T.C.L., Davies, P.J., Byrne, M., Williams, S., Manning, P., Pizarro, O., Thornborough, K., Woolsey, E., Thomas, A.L., Tudhope, A., 2008. From corals to canyons: the Great Barrier Reef margin. EOS Trans. Am. Geophys. Union 89 (24), 217–218.
Webster, J.M., Beaman, R.J., Puga-Bernabéu, Á., Ludman, D., Renema, W., Wust, R.A.J., George, N.P.J., Reimer, P.J., Jacobsen, G.E., Moss, P., 2012. Late Pleistocene history of turbidite sedimentation in a submarine canyon off the northern Great Barrier Reef, Australia. Palaeogeogr. Palaeoclimatol. Palaeoecol. 331-332, 75–89.
Xing, H.L., Ding, R.W., Yuen, D.A., 2014. Tsunami hazards along the Eastern Australian Coast from potential earthquakes: results from numerical simulations. Pure Appl. Geophys. 172 (8), 2087–2115.